

Bilayer t - J - J_{\perp} Model and Magnetically Mediated Pairing in the Pressurized Nickelate $\text{La}_3\text{Ni}_2\text{O}_7$

Xing-Zhou Qu,^{1,2,*} Dai-Wei Qu,^{1,2,*} Jialin Chen,^{2,3,*} Congjun Wu,^{4,5,6,7} Fan Yang,⁸ Wei Li,^{2,3,9,†} and Gang Su^{1,9,‡}

¹Kavli Institute for Theoretical Sciences, University of Chinese Academy of Sciences, Beijing 100190, China

²CAS Key Laboratory of Theoretical Physics, Institute of Theoretical Physics, Chinese Academy of Sciences, Beijing 100190, China

³Hefei National Laboratory, Hefei 230088, China

⁴New Cornerstone Science Laboratory, Department of Physics,

School of Science, Westlake University, 310024, Hangzhou, China

⁵Institute for Theoretical Sciences, Westlake University, 310024, Hangzhou, China

⁶Key Laboratory for Quantum Materials of Zhejiang Province,

School of Science, Westlake University, Hangzhou 310024, Zhejiang, China

⁷Institute of Natural Sciences, Westlake Institute for Advanced Study, 310024, Hangzhou, China

⁸School of Physics, Beijing Institute of Technology, Beijing 100081, China

⁹CAS Center for Excellence in Topological Quantum Computation,

University of Chinese Academy of Sciences, Beijing 100190, China

The recently discovered nickelate superconductor $\text{La}_3\text{Ni}_2\text{O}_7$ has a high transition temperature near 80 K under pressure, providing an additional avenue for exploring unconventional superconductivity. Here with state-of-the-art tensor-network methods, we study a bilayer t - J - J_{\perp} model for $\text{La}_3\text{Ni}_2\text{O}_7$ and find a robust s -wave superconductive (SC) order mediated by interlayer magnetic couplings. Large-scale density matrix renormalization group calculations find algebraic pairing correlations with Luttinger parameter $K_{\text{SC}} \lesssim 1$. Infinite projected entangled-pair state method obtains a nonzero SC order directly in the thermodynamic limit, and estimates a strong pairing strength $\bar{\Delta}_z \sim \mathcal{O}(0.1)$. Tangent-space tensor renormalization group simulations elucidate the temperature evolution of SC pairing and further determine a high SC temperature $T_c^*/J \sim \mathcal{O}(0.1)$. Because of the intriguing orbital selective behaviors and strong Hund's rule coupling in the compound, t - J - J_{\perp} model has strong interlayer spin exchange (while negligible interlayer hopping), which greatly enhances the SC pairing in the bilayer system. Such a magnetically mediated pairing has also been observed recently in the optical lattice of ultracold atoms. Our accurate and comprehensive tensor-network calculations reveal a robust SC order in the bilayer t - J - J_{\perp} model and shed light on the pairing mechanism of the high- T_c nickelate superconductor.

Introduction.— High- T_c superconductivity, since its discovery in doped cuprates [1–3], has raised long-lasting research interests. Very recently, under a high pressure of above 14 GPa, a Ruddlesden-Popper bilayer perovskite $\text{La}_3\text{Ni}_2\text{O}_7$ exhibits a high T_c near 80 K [4]. Later on, optical measurements show that the compound features strong electronic correlations that place it in the proximity of a Mott phase [5], despite certain density-wave-like order under ambient pressure. Zero resistance and strange metal behaviors have been reported under high pressure by other experimental groups [6, 7]. Currently, the electronic structure, effective model, and pairing mechanism in the pressurized nickelate $\text{La}_3\text{Ni}_2\text{O}_7$ are under very active investigation [8–17].

A bilayer two-orbital Hubbard model has been proposed to describe the high-pressure phase of $\text{La}_3\text{Ni}_2\text{O}_7$, where the kinetic part is determined from the density functional theory calculations [8], and the interactions including the Hubbard U , Hund's rule coupling J_H , etc., can be included. The SC instability and related pairing symmetry have been discussed with weak (to intermediate) coupling approaches [10–12]. Nevertheless, the large Coulomb interaction $U/t \gg 1$ in $\text{La}_3\text{Ni}_2\text{O}_7$ urgently calls for analysis from a strong coupling approach [13–15]. Precision many-body calculations are required to scrutinize the possible SC order in the effective model [16]. The tensor-network methods constitute a powerful and versatile approach for both ground-state [18–23] and finite-temperature properties [24–28] of correlated electrons. Unfortunately, the original bilayer two-orbital model

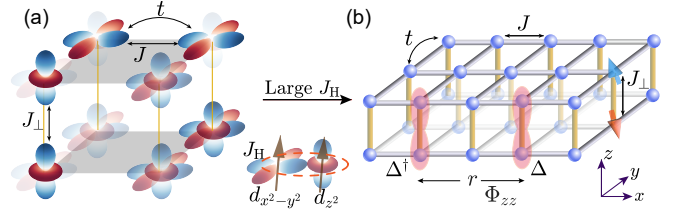


FIG. 1. (a) Two e_g orbitals in the bilayer structure of the nickelate $\text{La}_3\text{Ni}_2\text{O}_7$. The quarter-filled $d_{x^2-y^2}$ orbitals form an effective t - J model with intralayer hopping t and spin exchange J . The d_{z^2} orbital is localized and has an interlayer AF exchange through the σ bonding. The spins of $d_{x^2-y^2}$ and d_{z^2} orbitals are coupled through an on-site FM Hund's rule coupling J_H . In the large J_H limit, we arrive at (b) bilayer t - J - J_{\perp} model, where the interlayer AF coupling J_{\perp} is strong while the interlayer hopping is absent. The SC pairing correlation $\Phi_{zz}(r)$ is between two interlayer pairing $\Delta^{(\dagger)}$ along the vertical z direction and separated by a distance r along the x direction.

poses great challenges to tensor-network calculations and a dimension reduction in local Hilbert space while retaining the essence of electron correlations in the nickelate is very necessary.

Lately it is proposed that by considering the orbital selective behaviors of localized d_{z^2} and itinerant $d_{x^2-y^2}$ electrons, together with the strong ferromagnetic (FM) Hund's rule coupling, a bilayer t - J - J_{\perp} model with strong antiferromagnetic (AF) interlayer exchange J_{\perp} may provide an adequate effective model for $\text{La}_3\text{Ni}_2\text{O}_7$ [17]. Here we perform high-

precision ground-state and finite-temperature tensor-network calculations of this bilayer model, and reveal a robust SC order with high T_c that may account for the observation in the pressurized nickelate $\text{La}_3\text{Ni}_2\text{O}_7$.

Bilayer t - J - J_\perp model.— As shown in Fig. 1, we note the two e_g orbitals in $\text{La}_3\text{Ni}_2\text{O}_7$, namely, $d_{x^2-y^2}$ and d_{z^2} , have distinct and orbital selective behaviors [9]. The d_{z^2} orbital is almost localized with flat band structure promoted by the strong Hund’s couplings [14]. Considering that d_{z^2} orbital is only slightly doped (nearly half-filled) [13–15], we can freeze their charge fluctuations and regard the d_{z^2} electrons as local moments [14]. The interlayer σ bonding through the apical oxygen [4] renders a prominent interlayer AF coupling between the d_{z^2} moments (also dubbed as the “hidden dimer” [9]). On the other hand, the $d_{x^2-y^2}$ orbital is quarter-filled and adequately described by a t - J model within each layer [10, 12, 15]. The $d_{x^2-y^2}$ orbital has negligible interlayer single-particle tunneling [8, 9]. However, the strong FM Hund’s coupling can bind the two e_g orbitals and “passes” the strong interlayer AF coupling to the $d_{x^2-y^2}$ orbital [17], as illustrated in Fig. 1(a).

To see that, we start with the model $H = H_{t-J} + H_{\text{AF}} + H_{\text{Hund}}$, where H_{t-J} is the intralayer t - J model of $d_{x^2-y^2}$ electrons, and H_{AF} denotes the AF exchange $H_{\text{AF}} = J_\perp \sum_i \mathbf{S}_{i,\mu=1}^d \cdot \mathbf{S}_{i,\mu=-1}^d$ between the two layers. The index $\mu = \pm 1$ labels the upper(lower) layer, and \mathbf{S}^d denotes the localized d_{z^2} moment. $H_{\text{Hund}} = -J_H \sum_{i,\mu} \mathbf{S}_{i,\mu}^c \cdot \mathbf{S}_{i,\mu}^d$ is the on-site Hund’s coupling, with \mathbf{S}^c the spin of $d_{x^2-y^2}$ electron. To further simplify the two-orbital model, it is noted that the density functional theory calculations suggest $t \simeq 0.5$ eV ($d_{x^2-y^2}$), $t_\perp^z \simeq 0.64$ eV (d_{z^2}) [8, 9], placing the nickelate in the strong coupling regime by taking Hubbard $U \simeq 5$ eV (i.e., $U/t \sim 10$) [13, 14]. As an intra-atomic exchange, the FM Hund’s rule coupling is about $J_H \sim 1$ eV [13, 14], clearly greater than the spin exchanges $J \sim 4t^2/U \simeq 0.2$ eV and $J_\perp \simeq 0.32$ eV, which is sufficiently strong to transfer the AF couplings between the two e_g orbitals [29]. It is therefore sensible to take the large J_H limit and symmetrize the spins $\mathbf{S}_{i,\mu}^d$ and $\mathbf{S}_{i,\mu}^c$ of the two orbitals. The AF interlayer coupling between d_{z^2} moments can be effectively expressed as $\mathbf{S}_{i,\mu=1}^c \cdot \mathbf{S}_{i,\mu=-1}^c$ in the symmetrized spin-triplet space. With this, an effective single-band bilayer t - J - J_\perp model can be obtained [17]

$$\begin{aligned}
H_{\text{bilayer}} = & -t \sum_{\langle i,j \rangle, \mu, \sigma} (c_{i,\mu,\sigma}^\dagger c_{j,\mu,\sigma} + H.c.) \\
& + J \sum_{\langle i,j \rangle, \mu} (\mathbf{S}_{i,\mu}^c \cdot \mathbf{S}_{j,\mu}^c - \frac{1}{4} n_{i,\mu} n_{j,\mu}) \\
& + J_\perp \sum_i \mathbf{S}_{i,\mu=1}^c \cdot \mathbf{S}_{i,\mu=-1}^c, \quad (1)
\end{aligned}$$

where $\sigma = \{\uparrow, \downarrow\}$ is the spin orientation, and the vector operator $\mathbf{S}_{i,\mu}^c = \frac{1}{2} c_{i,\mu,\sigma}^\dagger (\boldsymbol{\sigma}_{\sigma,\sigma'}) c_{i,\mu,\sigma'}$ denotes the spin of the itinerant $d_{x^2-y^2}$ electron with the Pauli matrices $\boldsymbol{\sigma} = \{\sigma_x, \sigma_y, \sigma_z\}$. Note the double occupancy is projected out in the t - J - J_\perp model as usual.

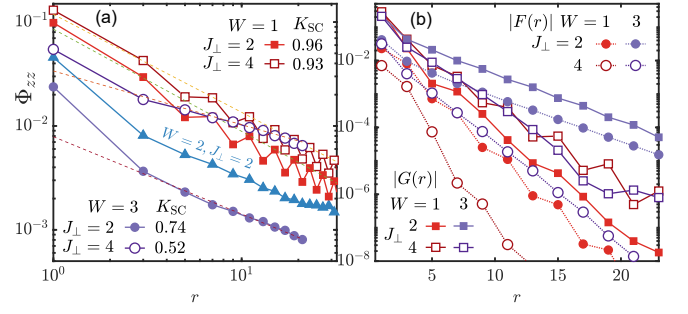


FIG. 2. (a) Pairing correlation Φ_{zz} on the $2 \times W \times L$ bilayer lattices with widths $1 \leq W \leq 3$ and long length L , namely, $2 \times 1 \times 128$ ($W = 1, n_e = 0.5$), $2 \times 2 \times 64$ ($W = 2, n_e \approx 0.54$), and $2 \times 3 \times 48$ ($W = 3, n_e = 0.5$). The SC correlations exhibit algebraic behaviors as $\Phi_{zz}(r) \sim r^{-K_{\text{SC}}}$, enhanced with interlayer coupling J_\perp . The $W = 2$ data fall into algebraic scaling with oscillations [31], leading to inaccurate extraction of the Luttinger parameters. (b) Spin-spin correlation $F(r)$ and the single-particle Green’s function $G(r)$ decay exponentially (see definitions in the main text) in the SC phase [32].

Below we consider the intralayer hopping $t = 3$ and spin exchange $J = 1$ (taken as energy scale henceforth), and the interlayer AF couplings J_\perp is varied to explore the SC and possibly competing charge density wave (CDW) orders. Interlayer hopping t_\perp is forbidden [except in Fig. 3(c)], different from the previously studied bilayer Hubbard-like models [30]. As the $d_{x^2-y^2}$ orbitals are nearly quarter-filled, we set $n_e = 0.5$ and the hole density $n_h = 1 - n_e = 0.5$ in the pristine $\text{La}_3\text{Ni}_2\text{O}_7$.

Tensor-network methods for zero- and finite-temperature properties.— To simulate the bilayer model in Eq. (1), we employ tensor-network approaches for both $T = 0$ and $T > 0$ calculations. Regarding the ground state, we exploit the density matrix renormalization group (DMRG) [18, 19] for the finite-size systems and the infinite projected entangled-pair state (iPEPS) directly in the thermodynamic limit [20–23]. In DMRG we map the $2 \times W \times L$ bilayer system into a quasi-1D chain with long-range interactions [31], and implement the non-Abelian and Abelian symmetries with tensor libraries [33–36]. We retain up to $D^* = 12000 \text{ U}(1)_{\text{charge}} \times \text{SU}(2)_{\text{spin}}$ multiplets (equivalently $D \simeq 30000$ individual states), which well converge the results [31]. For iPEPS calculations, we adopt the simple update [37, 38] with retained bond dimension up to $D = 12$, which is extrapolated to infinite D and compared to the DMRG results. Moreover, we exploit the finite- T tensor networks, in particular the recently developed tangent-space tensor renormalization group [26] to study the bilayer system with $W = 1$ and length up to $L = 128$. Up to $D^* = 1600 \text{ U}(1)_{\text{charge}} \times \text{SU}(2)_{\text{spin}}$ multiplets (equivalently $D \simeq 3600$ states) render very well converged results down to a low temperature $T/J \simeq 0.1$ [31].

Robust SC order and magnetically mediated interlayer pairing.— In Fig. 2 we show the DMRG results of pairing correlations $\Phi_{zz}(r) = \langle \Delta_i^\dagger \Delta_j \rangle$ with interlayer pairing $\Delta_i^\dagger = \frac{1}{\sqrt{2}} \sum_{\mu=\pm 1} c_{i,\mu,\uparrow}^\dagger c_{i,-\mu,\downarrow}^\dagger$ and distance $r \equiv |j - i|$, where we

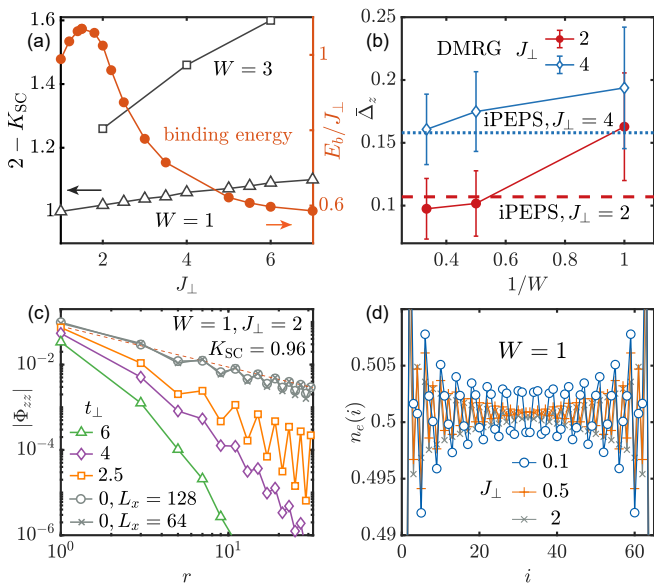


FIG. 3. (a) The Luttinger parameter ($2 - K_{\text{SC}}$) vs. J_{\perp} calculated at various bilayer systems. The binding energy for $W = 1$ system is also shown. (b) The SC order parameter $\bar{\Delta}_z$ obtained with iPEPS (dashed horizontal lines) and DMRG (solid lines) for $J_{\perp} = 2, 4$. In the latter, $\bar{\Delta}_z$ is estimated within central columns, and the error bars represent the difference between the maximal and minimal values by varying the number of columns involved. We set $n_e = 0.5$ for the $W = 1, 3$ cases, while for the $W = 2$ case it is shifted slightly to $n_e \simeq 0.54$. (c) Pairing correlation $|\Phi_{zz}|$ with various interlayer hopping t_{\perp} . For the $t_{\perp} = 0$ case, we show the pairing correlations in excellent data convergence as computed with $L_x = 64$ and 128 . (d) The electron density profiles $n_e(i)$, $1 \leq i \leq L$ for various J_{\perp} computed on the $2 \times 1 \times 64$ system.

find $\Phi_{zz}(r)$ shows algebraic scaling with the Luttinger exponent $K_{\text{SC}} \lesssim 1$ for moderate to strong J_{\perp} . In Fig. 2(b), we calculate the spin-spin correlation $F(r) = \frac{1}{2} \sum_{\mu} \langle \mathbf{S}_{i,\mu}^c \cdot \mathbf{S}_{j,\mu}^c \rangle$ and the Green's function $G(r) = \frac{1}{4} \sum_{\mu,\sigma} \langle c_{i,\mu,\sigma}^{\dagger} c_{j,\mu,\sigma} + \text{H.c.} \rangle$, and find both correlations decay exponentially. The DMRG results in Fig. 2 indicate the emergence of Luther-Emery liquid [39] with quasi-long-range SC order, as well as finite spin and single-particle gaps.

The AF exchange J_{\perp} plays an essential role in mediating the interlayer pairing and forming the rung-singlet SC phase [40]. In Fig. 3(a), we provide the DMRG results of the Luttinger parameter K_{SC} controlling the scaling behaviors of pairing correlations. We find $(2 - K_{\text{SC}}) \gtrsim 1$ increases rapidly with J_{\perp} and signifies a diverging susceptibility at low temperature as $\chi_{\text{SC}} \sim 1/T^{(2-K_{\text{SC}})}$. The pairing susceptibility $\chi_{\text{SC}} = \frac{2}{N} \partial \langle \Delta_{\text{tot}} \rangle_{\beta} / \partial h_p$ measures the response of SC order parameter to a small pairing field h_p coupled to $\Delta_{\text{tot}} = \frac{1}{2} \sum_i (\Delta_i + \Delta_i^{\dagger})$. To further characterize the enhancement of pairing strength, we compute the binding energy $E_b = E(N_e + 1) + E(N_e - 1) - 2E(N_e)$, where $E(N_e)$ is the ground-state energy with N_e electrons. In Fig. 3(a), we find E_b increases with J_{\perp} as the ratio $E_b/J_{\perp} \gtrsim 0.6$. However, E_b/J_{\perp} is not monotonic and has a round peak at $J_{\perp} \approx 1.5$.

In the strong J_{\perp} limit the escalation of binding energy slows down its pace and the ratio converges to $E_b/J_{\perp} \simeq 0.6$.

With iPEPS calculations directly in the thermodynamic limit where symmetry breaking is allowed to occur, we evaluate the SC order parameter $\bar{\Delta}_z = \langle \Delta_i^{\dagger} \rangle$ averaged over the two sublattices, and show the results in Fig. 3(b). We find $\bar{\Delta}_z$ increases with J_{\perp} and reaches about 0.11 for $J_{\perp} = 2$ and 0.16 for $J_{\perp} = 4$. In Fig. 3(b) we also show the DMRG estimation of the order parameter $\bar{\Delta}_z = \sqrt{\frac{1}{N_b} \sum_{i,j} \langle \Delta_i^{\dagger} \Delta_j \rangle}$ where i, j are restricted within N_c central columns, and N_b is number of the credited pairs. In practice, we vary N_c from 8 to 16 for different lattice geometries, and find the DMRG and iPEPS results agree well. Notice that the order parameter $\bar{\Delta}_z$ of the bilayer t - J - J_{\perp} system [$\mathcal{O}(10^{-1})$] is much greater than that found in the plain t - J square lattice [$\mathcal{O}(10^{-2})$] [41].

The order parameter $\bar{\Delta}_z$ and pairing correlations are found to be uniform in each layer, i.e., it belongs to an s -wave SC order. We have also computed the intralayer pairings Φ_{yy} and Φ_{yx} with DMRG, and the order parameters $\bar{\Delta}_{x,y}$ with iPEPS [31], which are found to be negligibly small when compared to Φ_{zz} (and $\bar{\Delta}_z$). Based on the results in Figs. 2 and 3, we conclude there exists a robust rung-singlet SC order mediated and enhanced by magnetic couplings J_{\perp} in the bilayer t - J - J_{\perp} model for $\text{La}_3\text{Ni}_2\text{O}_7$.

Pauli blocking and charge density-wave instability.— The existence of strong interlayer J_{\perp} while absence of hopping t_{\perp} is a key for the robust SC order to appear in the bilayer system. In Fig. 3(c) we artificially introduce the interlayer hopping t_{\perp} , and find the SC order gets weakened and even suppressed as t_{\perp} increases. This can be ascribed to the Pauli blocking effect where the holes tend to repel each other kinetically according to their hopping amplitude [42], spoiling the interlayer pairing for strong t_{\perp} . Moreover, this observation may also be relevant to the experiments: further increasing pressure in the SC phase of $\text{La}_3\text{Ni}_2\text{O}_7$ does not enhance T_c but decreases it [4, 6, 7]. It is possible that high pressure enhances interlayer tunneling of the $d_{x^2-y^2}$ orbitals and thus weakens the SC order.

In Fig. 3(d), we show the electron density distribution $n_e(i)$ by tuning J_{\perp} to smaller values. For $J_{\perp} = 2$, the CDW fluctuation is rather weak, consistent with a robust s -wave SC state. However, for smaller J_{\perp} the SC order becomes weakened, while the CDW instability turns strong. This may explain the absence of SC order in $\text{La}_3\text{Ni}_2\text{O}_7$ under ambient pressure, where certain density-wave-like instability has been observed in recent experiments [5–7]. The change of interlayer Ni-O-Ni bond angle [from 168° (ambient) to 180° (pressurized)] and length (by 1.9 \AA) may sensitively influence J_{\perp} , thus switching between the CDW and SC phases. Moreover, by reducing the hole density we find even clearer CDW pattern [31], suggesting that the CDW instability or stripe phase may also be a competing order in the bilayer nickelate.

Finite-temperature pairing and magnetic susceptibilities.— In Fig. 4 we show the temperature evolutions of spin and pairing correlations. Firstly, from Fig. 4(a) we find the elec-

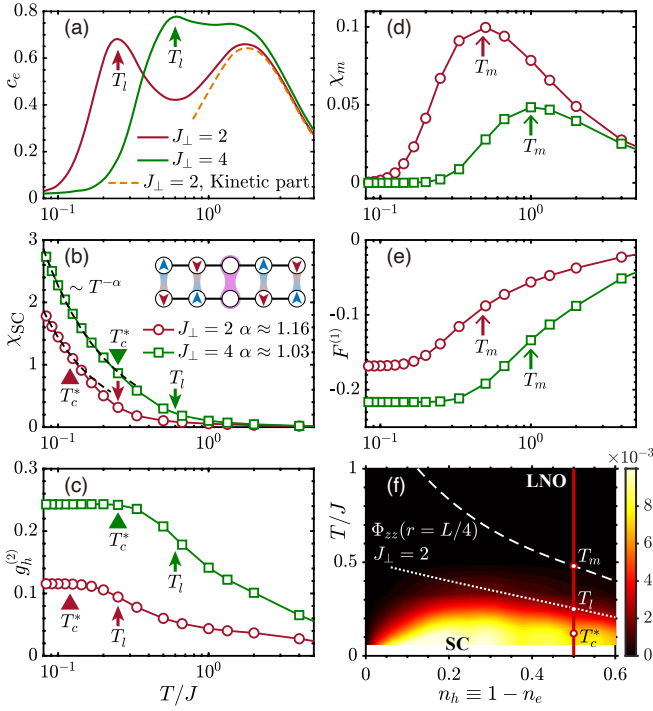


FIG. 4. Finite-temperature results for $W = 1$ systems with length up to $L = 128$. In panels (a)-(e), the data for $J_{\perp} = 2$ (red lines) and 4 (green) are shown. In (a),(c)-(e) the hole density is fixed as $n_h \equiv 1 - n_e = 0.5$, and in (b) the data are calculated with fine-tuned chemical potential that leads to $n_h \simeq 0.5$. (a) shows the specific heat c_e with T_l the lower characteristic temperature. (b) shows the pairing susceptibility χ_{SC} , which diverges with a power-law scaling $T^{-\alpha}$ (the dashed lines) for $T \leq T_c^*$. The interlayer pairing and AF correlations are illustrated in the inset. (c) shows the interlayer hole correlations on the rungs, with T_l and T_c^* determined from (a) and (b), respectively. (d) shows the magnetic susceptibility χ_m with a hump at T_m . (e) shows the rung spin correlations. (f) The contour plot of the pairing correlation $\Phi_{zz}(r = L/4)$ for various hole densities n_h computed with $J_{\perp} = 2$. The vertical red line denotes the $n_h = 0.5$ case relevant for $\text{La}_3\text{Ni}_2\text{O}_7$ (LNO).

tron specific heat $c_e = \frac{1}{N_e} \frac{\partial \varepsilon}{\partial T}$ exhibits a double-peak structure, with the higher- T peak contributed by the kinetic energy, and lower- T scale responsible for SC pairing labeled by T_l . In Fig. 4(b) we apply a uniform pairing field $-h_p \Delta_{\text{tot}}$ with $h_p = 2 \times 10^{-3}$, and compute the pairing susceptibility. We find that χ_{SC} is rather small for $T > T_l$ and becomes significant for $T < T_l$, making T_l the SC-fluctuation onset temperature.

As temperature further lowers, we find χ_{SC} exhibits an algebraic divergence $\chi_{SC} \sim T^{-\alpha}$ for temperature below T_c^* , when the system enters the low-temperature SC regime. The fitted exponent in Fig. 4(b) is $\alpha \simeq 1$, consistent with the ground-state DMRG results of $K_{SC} \simeq 1$ for $W = 1$. Both T_l and T_c^* increase with J_{\perp} , and in Fig. 4(a) we find $T_l/J \simeq 0.25$ for $J_{\perp} = 2$, which is enhanced to $T_l/J \simeq 0.6$ for $J_{\perp} = 4$. Similarly in Fig. 4(b) the χ_{SC} curves show an overall enhancement, and the T_c^*/J increases from 0.12 for $J_{\perp} = 2$

to about 0.25 for $J_{\perp} = 4$. In Fig. 4(c) we show the hole-hole correlation $g_h^{(2)} = (2/N) \sum_i \langle h_{i,\mu=1} h_{i,\mu=-1} \rangle_{\beta} / (\langle h_{i,\mu=1} \rangle_{\beta} \cdot \langle h_{i,\mu=-1} \rangle_{\beta}) - 1$, where N is the number of lattice sites with $h_{i,\mu}$ the hole density operator. The positive $g_h^{(2)}$ indicates the attractive (“bunching”) correlations between the holes. From Fig. 4(c), we find $g_h^{(2)}$ rapidly increases at about T_l and saturates at about T_c^* when the pairing susceptibility starts to diverge algebraically in Fig. 4(b).

To further reveal the intriguing interplay between antiferromagnetism and superconductivity in the bilayer system, we compute the magnetic susceptibility χ_m and rung spin-spin correlation $F^{(1)} = \frac{2}{N} \sum_i \langle \mathbf{S}_{i,\mu=1} \cdot \mathbf{S}_{i,\mu=-1} \rangle_{\beta}$ in Fig. 4(d),(e). The magnetic susceptibility χ_m becomes suppressed below T_m in Fig. 4(d), which can be ascribed to the rapid establishment of correlation $F^{(1)}$ at about the same temperature [Fig. 4(e)].

Temperature evolution of the SC order.— Now we summarize the temperature evolution of the pairing correlations in Fig. 4(f), where the red line denotes $\text{La}_3\text{Ni}_2\text{O}_7$ with hole density $n_h \equiv 1 - n_e \simeq 0.5$. As temperature lowers, the interlayer AF correlation develops at about $T_m/J \simeq 0.48$, and then the hole bunching occurs at $T_l/J \simeq 0.25$, shortly after that the system enters the coherent regime below $T_c^*/J \simeq 0.12$, establishing eventually the quasi-long-range SC order.

As shown in Fig. 4(f), by doping electrons into the system (or via a self-doping from d_{z^2} to the $d_{x^2-y^2}$ orbitals), the SC order and its characteristic temperature can be further enhanced. For $J_{\perp} = 2$, the optimal hole density appears at $n_h \sim 0.25$, to the electron-doping side of $\text{La}_3\text{Ni}_2\text{O}_7$, as also evidenced by the enhanced pairing susceptibility and temperature scales T_l and T_c^* [31].

Discussion and outlook.— We exploit multiple tensor-network methods and reveal robust s -wave SC order in the bilayer t - J - J_{\perp} model for the recently discovered nickelate superconductor. In $\text{La}_3\text{Ni}_2\text{O}_7$ the $d_{x^2-y^2}$ orbital has a hole density of $n_h \simeq 0.5$ — a large value on the verge of quenching the SC in cuprates. For the latter, large hole doping may undermine the intralayer AF correlations and suppress the SC order. Surprisingly, in $\text{La}_3\text{Ni}_2\text{O}_7$ the SC order remains robust and has a high $T_c \simeq 80$ K even with large hole density. Based on our t - J - J_{\perp} model calculations, we ascribe it to the robust pairing mechanism mediated by strong interlayer AF exchange. In Fig. 4(f), we find indeed the SC dome can extend to a very wide regime up to $n_h \sim 0.6$ for the bilayer nickelate.

We would also point out an intriguing and rather unexpected connection between the high- T_c nickelate and ultracold atom systems. Recently, the mixed dimensional (mixD) bilayer optical lattices with strong interlayer spin exchange while no interlayer single-particle tunneling has been realized [42, 43]. Remarkably, such a t - J - J_{\perp} mixD bilayer model naturally emerges in the orbital-selective nickelate $\text{La}_3\text{Ni}_2\text{O}_7$: The $d_{x^2-y^2}$ electrons are itinerant within each layer, while d_{z^2} orbitals are nearly half-filled and localized. The FM Hund’s coupling “glues” the spins of two e_g orbitals, conveying to

the $d_{x^2-y^2}$ electrons a strong AF coupling—the driving force for the interlayer pairing. To thoroughly validate our effective model for $\text{La}_3\text{Ni}_2\text{O}_7$, a detailed analysis of the two-orbital bilayer model with realistic parameters is necessary. Our preliminary results support the scenario proposed here [29].

Overall, our results provide a solid and valuable basis for understanding the unconventional SC in pressurized $\text{La}_3\text{Ni}_2\text{O}_7$ from a strong coupling approach, and put various experimental observations in a coherent picture. They offer useful guidance for future studies in the nickelate superconductors and also mixD ultracold atom systems.

W.L. and F.Y. are indebted to Yang Qi and Qiaoyi Li for stimulating discussions. This work was supported by the National Natural Science Foundation of China (Grants No. 12222412, No. 11834014, No. 11974036, No. 12047503, No. 12074031, No. 12174317, and No. 12234016), Strategic Priority Research Program of CAS (Grant No. XDB28000000), Innovation Program for Quantum Science and Technology (No. 2021ZD0301800 and No. 2021ZD0301900), the New Cornerstone Science Foundation, and CAS Project for Young Scientists in Basic Research (Grant No. YSBR-057). We thank the HPC-ITP for the technical support and generous allocation of CPU time.

* These authors contributed equally to this work.

† w.li@itp.ac.cn

‡ gsu@ucas.ac.cn

- [1] J. G. Bednorz and K. A. Müller, Possible high- T_c superconductivity in the Ba-La-Cu-O system, *Z. Phys. B Condens. Matter* **64**, 189 (1986).
- [2] P. A. Lee, N. Nagaosa, and X.-G. Wen, Doping a mott insulator: Physics of high-temperature superconductivity, *Rev. Mod. Phys.* **78**, 17 (2006).
- [3] B. Keimer, S. A. Kivelson, M. R. Norman, S. Uchida, and J. Zaanen, From quantum matter to high-temperature superconductivity in copper oxides, *Nature (London)* **518**, 179 (2015).
- [4] H. Sun, M. Huo, X. Hu, J. Li, Z. Liu, Y. Han, L. Tang, Z. Mao, P. Yang, B. Wang, J. Cheng, D.-X. Yao, G.-M. Zhang, and M. Wang, Signatures of superconductivity near 80 K in a nickelate under high pressure, *Nature (London)* **621**, 493 (2023).
- [5] Z. Liu, M. Huo, J. Li, Q. Li, Y. Liu, Y. Dai, X. Zhou, J. Hao, Y. Lu, M. Wang, and H.-H. Wen, Electronic correlations and energy gap in the bilayer nickelate $\text{La}_3\text{Ni}_2\text{O}_7$ (2023), [arXiv:2307.02950](https://arxiv.org/abs/2307.02950).
- [6] J. Hou, P. T. Yang, Z. Y. Liu, J. Y. Li, P. F. Shan, L. Ma, G. Wang, N. N. Wang, H. Z. Guo, J. P. Sun, Y. Uwatoko, M. Wang, G. M. Zhang, B. S. Wang, and J. G. Cheng, Emergence of high-temperature superconducting phase in the pressurized $\text{La}_3\text{Ni}_2\text{O}_7$ crystals (2023), [arXiv:2307.09865](https://arxiv.org/abs/2307.09865).
- [7] Y. Zhang, D. Su, Y. Huang, H. Sun, M. Huo, Z. Shan, K. Ye, Z. Yang, R. Li, M. Smidman, M. Wang, L. Jiao, and H. Yuan, High-temperature superconductivity with zero-resistance and strange metal behavior in $\text{La}_3\text{Ni}_2\text{O}_7$ (2023), [arXiv:2307.14819](https://arxiv.org/abs/2307.14819).
- [8] Z. Luo, X. Hu, M. Wang, W. Wú, and D.-X. Yao, Bilayer two-orbital model of $\text{La}_3\text{Ni}_2\text{O}_7$ under pressure, *Phys. Rev. Lett.* **131**, 126001 (2023).
- [9] Y. Zhang, L.-F. Lin, A. Moreo, and E. Dagotto, Electronic structure, dimer physics, orbital-selective behavior, and magnetic tendencies in the bilayer nickelate superconductor $\text{La}_3\text{Ni}_2\text{O}_7$ under pressure, *Phys. Rev. B* **108**, L180510 (2023).
- [10] Q.-G. Yang, D. Wang, and Q.-H. Wang, Possible s_{\pm} -wave superconductivity in $\text{La}_3\text{Ni}_2\text{O}_7$, *Phys. Rev. B* **108**, L140505 (2023).
- [11] H. Sakakibara, N. Kitamine, M. Ochi, and K. Kuroki, Possible high t_c superconductivity in $\text{La}_3\text{Ni}_2\text{O}_7$ under high pressure through manifestation of a nearly-half-filled bilayer Hubbard model (2023), [arXiv:2306.06039](https://arxiv.org/abs/2306.06039).
- [12] Y. Gu, C. Le, Z. Yang, X. Wu, and J. Hu, Effective model and pairing tendency in bilayer Ni-based superconductor $\text{La}_3\text{Ni}_2\text{O}_7$ (2023), [arXiv:2306.07275](https://arxiv.org/abs/2306.07275).
- [13] V. Christiansson, F. Petocchi, and P. Werner, Correlated electronic structure of $\text{La}_3\text{Ni}_2\text{O}_7$ under pressure, *Phys. Rev. Lett.* **131**, 206501 (2023).
- [14] Y. Cao and Y.-F. Yang, Flat bands promoted by Hund's rule coupling in the candidate double-layer high-temperature superconductor $\text{La}_3\text{Ni}_2\text{O}_7$ (2023), [arXiv:2307.06806](https://arxiv.org/abs/2307.06806).
- [15] W. Wú, Z. Luo, D.-X. Yao, and M. Wang, Charge transfer and Zhang-Rice singlet bands in the nickelate superconductor $\text{La}_3\text{Ni}_2\text{O}_7$ under pressure (2023), [arXiv:2307.05662](https://arxiv.org/abs/2307.05662).
- [16] Y. Shen, M. Qin, and G.-M. Zhang, Effective bi-layer model Hamiltonian and density-matrix renormalization group study for the high- t_c superconductivity in $\text{La}_3\text{Ni}_2\text{O}_7$ under high pressure, *Chin. Phys. Lett.* **40**, 127401 (2023).
- [17] C. Lu, Z. Pan, F. Yang, and C. Wu, Interlayer coupling driven high-temperature superconductivity in $\text{La}_3\text{Ni}_2\text{O}_7$ under pressure (2023), [arXiv:2307.14965](https://arxiv.org/abs/2307.14965).
- [18] S. R. White, Density matrix formulation for quantum renormalization groups, *Phys. Rev. Lett.* **69**, 2863 (1992).
- [19] U. Schollwöck, The density-matrix renormalization group in the age of matrix product states, *Ann. Phys. (Amsterdam)* **326**, 96 (2011).
- [20] F. Verstraete and J. I. Cirac, Renormalization algorithms for quantum-many body systems in two and higher dimensions (2004), [arXiv:cond-mat/0407066](https://arxiv.org/abs/cond-mat/0407066).
- [21] J. I. Cirac, D. Pérez-García, N. Schuch, and F. Verstraete, Matrix product states and projected entangled pair states: Concepts, symmetries, theorems, *Rev. Mod. Phys.* **93**, 045003 (2021).
- [22] P. Corboz, R. Orús, B. Bauer, and G. Vidal, Simulation of strongly correlated fermions in two spatial dimensions with fermionic projected entangled-pair states, *Phys. Rev. B* **81**, 165104 (2010).
- [23] J. Jordan, R. Orús, G. Vidal, F. Verstraete, and J. I. Cirac, Classical simulation of infinite-size quantum lattice systems in two spatial dimensions, *Phys. Rev. Lett.* **101**, 250602 (2008).
- [24] W. Li, S.-J. Ran, S.-S. Gong, Y. Zhao, B. Xi, F. Ye, and G. Su, Linearized tensor renormalization group algorithm for the calculation of thermodynamic properties of quantum lattice models, *Phys. Rev. Lett.* **106**, 127202 (2011).
- [25] B.-B. Chen, L. Chen, Z. Chen, W. Li, and A. Weichselbaum, Exponential thermal tensor network approach for quantum lattice models, *Phys. Rev. X* **8**, 031082 (2018).
- [26] Q. Li, Y. Gao, Y.-Y. He, Y. Qi, B.-B. Chen, and W. Li, Tangent space approach for thermal tensor network simulations of the 2D Hubbard model, *Phys. Rev. Lett.* **130**, 226502 (2023).
- [27] B.-B. Chen, C. Chen, Z. Chen, J. Cui, Y. Zhai, A. Weichselbaum, J. von Delft, Z. Y. Meng, and W. Li, Quantum many-body simulations of the two-dimensional Fermi-Hubbard model in ultracold optical lattices, *Phys. Rev. B* **103**, L041107 (2021).
- [28] X. Lin, B.-B. Chen, W. Li, Z. Y. Meng, and T. Shi, Exciton pro-

- liferation and fate of the topological Mott insulator in a twisted bilayer graphene lattice model, *Phys. Rev. Lett.* **128**, 157201 (2022).
- [29] X.-Z. Qu, D.-W. Qu, W. Li, and G. Su, Roles of Hund's rule and hybridization in the two-orbital model for High- T_c superconductivity in the bilayer nickelate (2023), [arXiv:2311.12769](https://arxiv.org/abs/2311.12769).
- [30] T. A. Maier and D. J. Scalapino, Pair structure and the pairing interaction in a bilayer Hubbard model for unconventional superconductivity, *Phys. Rev. B* **84**, 180513 (R) (2011).
- [31] Supplementary Sec. I introduces the many-body calculation methods, including the DMRG, iPEPS, and tanTRG exploited in this work, and Sec. II provides supplemental data for the ground-state and finite-temperature properties, which includes Refs. [44–48].
- [32] We compute the spin, charge, and SC pairing correlations on a pair of sites separated by distance r and symmetric around the center of the system to avoid boundary effects.
- [33] A. Weichselbaum, Non-abelian symmetries in tensor networks : A quantum symmetry space approach, *Ann. Phys. (Amsterdam)* **327**, 2972 (2012).
- [34] A. Weichselbaum, X-symbols for non-Abelian symmetries in tensor networks, *Phys. Rev. Res.* **2**, 023385 (2020).
- [35] M. Fishman, S. R. White, and E. M. Stoudenmire, The ITensor software library for tensor network calculations, *SciPost Phys. Codebases* , 4 (2022).
- [36] M. Fishman, S. R. White, and E. M. Stoudenmire, Codebase release 0.3 for ITensor, *SciPost Phys. Codebases* , 4 (2022).
- [37] H. C. Jiang, Z. Y. Weng, and T. Xiang, Accurate determination of tensor network state of quantum lattice models in two dimensions, *Phys. Rev. Lett.* **101**, 090603 (2008).
- [38] W. Li, J. von Delft, and T. Xiang, Efficient simulation of infinite tree tensor network states on the bethe lattice, *Phys. Rev. B* **86**, 195137 (2012).
- [39] A. Luther and V. J. Emery, Backward scattering in the one-dimensional electron gas, *Phys. Rev. Lett.* **33**, 589 (1974).
- [40] W. Wu, M. Ferrero, A. Georges, and E. Kozik, Controlling Feynman diagrammatic expansions: Physical nature of the pseudogap in the two-dimensional Hubbard model, *Phys. Rev. B* **96**, 041105(R) (2017).
- [41] P. Corboz, T. M. Rice, and M. Troyer, Competing states in the t - J model: Uniform d -wave state versus stripe state, *Phys. Rev. Lett.* **113**, 046402 (2014).
- [42] S. Hirthe, T. Chalopin, D. Bourgund, P. Bojović, A. Bohrdt, E. Demler, F. Grusdt, I. Bloch, and T. A. Hilker, Magnetically mediated hole pairing in fermionic ladders of ultracold atoms, *Nature (London)* **613**, 463 (2023).
- [43] A. Bohrdt, L. Homeier, I. Bloch, E. Demler, and F. Grusdt, Strong pairing in mixed-dimensional bilayer antiferromagnetic Mott insulators, *Nat. Phys.* **18**, 651 (2022).
- [44] X. Lu, D.-W. Qu, Y. Qi, W. Li, and S.-S. Gong, Ground-state phase diagram of the extended two-leg t - J ladder, *Phys. Rev. B* **107**, 125114 (2023).
- [45] P. Corboz and G. Vidal, Fermionic multiscale entanglement renormalization ansatz, *Phys. Rev. B* **80**, 165129 (2009).
- [46] T. Barthel, C. Pineda, and J. Eisert, Contraction of fermionic operator circuits and the simulation of strongly correlated fermions, *Phys. Rev. A* **80**, 042333 (2009).
- [47] C. V. Kraus, N. Schuch, F. Verstraete, and J. I. Cirac, Fermionic projected entangled pair states, *Phys. Rev. A* **81**, 052338 (2010).
- [48] R. Orús and G. Vidal, Simulation of two-dimensional quantum systems on an infinite lattice revisited: Corner transfer matrix for tensor contraction, *Phys. Rev. B* **80**, 094403 (2009).

Supplemental Materials for

Bilayer t - J - J_{\perp} Model and Magnetically Mediated Pairing in the Pressurized Nickelate $\text{La}_3\text{Ni}_2\text{O}_7$

Qu *et al.*

I. ZERO AND FINITE-TEMPERATURE SIMULATION METHODS

In this work, we employ the density matrix renormalization group (DMRG) and infinite projected entangled-pair state (iPEPS) for the ground state, as well as the tangent-space tensor renormalization group (tanTRG) for finite-temperature properties of the bilayer t - J - J_{\perp} model.

A. DMRG Calculations

In the DMRG calculations, two different tensor-network libraries have been employed. We exploit QSpace library [33, 34] to implement $U(1)_{\text{charge}} \times SU(2)_{\text{spin}}$ symmetry in our DMRG code. ITensors library [35, 36] is also utilized to perform a $U(1)_{\text{charge}} \times U(1)_{\text{spin}}$ DMRG as a double check. For example, in the $2 \times 1 \times 128$ systems we keep up to 2000 $U(1)_{\text{charge}} \times SU(2)_{\text{spin}}$ multiplets, which ensures a small truncation error $\lesssim 10^{-11}$. In the $2 \times 3 \times 48$ systems we keep up to 12 000 $U(1)_{\text{charge}} \times SU(2)_{\text{spin}}$ multiplets with typical truncation error $\sim 5 \times 10^{-6}$. In the calculations, D represents the number of $U(1)_{\text{charge}} \times U(1)_{\text{spin}}$ states and D^* for the $U(1)_{\text{charge}} \times SU(2)_{\text{spin}}$ multiplets.

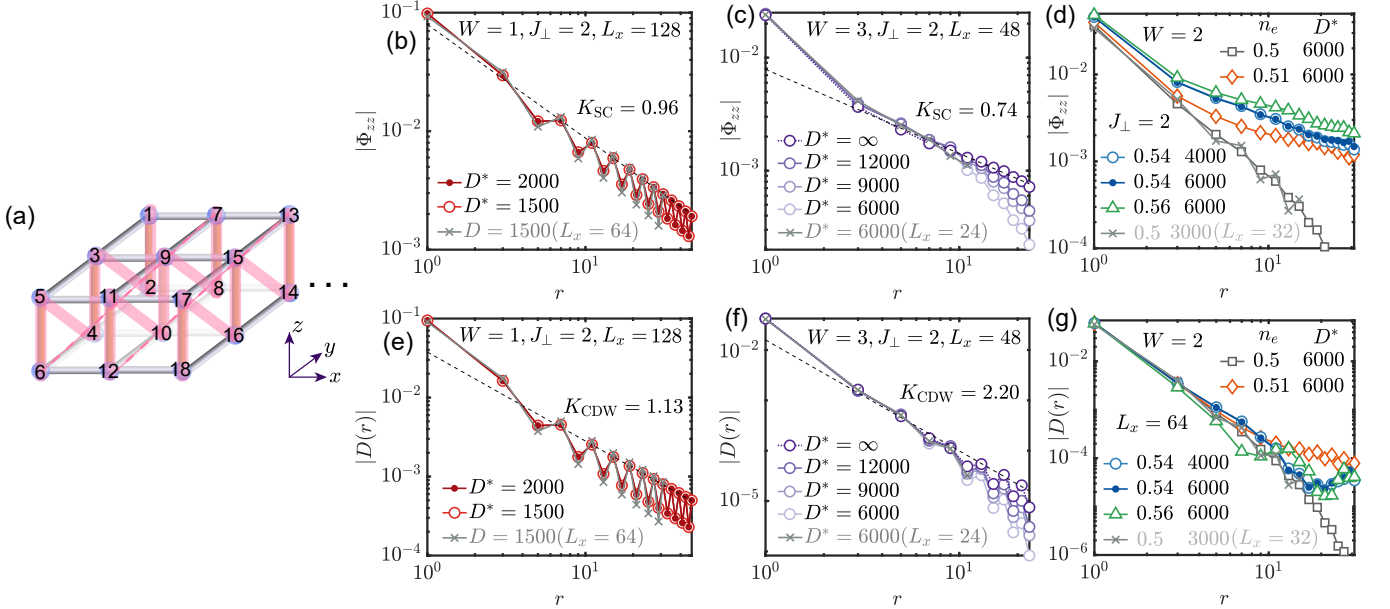


FIG. S1. (a) Illustration of the zigzag path used in DMRG calculation, and the model parameters are chosen as $J_{\perp} = 2$, $J = 1$, and $t = 3$. The DMRG results on the t - J - J_{\perp} model on the $2 \times W \times L_x$ lattices with longer L_x are shown in (b-g). The (b,c,d) panels show the pairing correlations $\Phi_{zz}(r) = \langle \Delta_i^{\dagger} \Delta_j \rangle$ and (e,f,g) show the charge correlations $D(r) = \langle n_i n_j \rangle - \langle n_i \rangle \langle n_j \rangle$, with $r \equiv |i - j|$. We show $W = 1, 2, 3$ systems with relatively long L_x up to 128. As a comparison, the results with shorter length L_x are displayed with grey lines and cross markers. Note that for $W = 1, 3$ cases, the Luttinger parameters K_{SC} and K_{CDW} can be accurately extracted. On the other hand, though the $W = 2$ data fall into algebraic decay, they are highly oscillating and lead to inaccurate extractions of the Luttinger parameters.

Data convergence.— In Fig. S1 we compare the results obtained in different system sizes and bond dimensions to confirm the convergence of our ground-state simulations. The pairing and charge correlations are presented in Fig. S1 for $J_{\perp} = 2$ and in Fig. S2 for $J_{\perp} = 4, 6$ systems. For the $W = 1$ case [Fig. S1(b,e) and Fig. S2(a, d)], we find the data are fully converged by retaining $D^* = 2000$ (equivalently $D \approx 4400$ individual states), from which we can extract the Luttinger parameters K_{SC} and K_{CDW} accurately. For the $W = 3$ case shown in Fig. S1(c,f), we retain up to 12 000 bond multiplets, and find that the correlations are converged for short distances. For longer distances, we perform a fitting with polynomial function

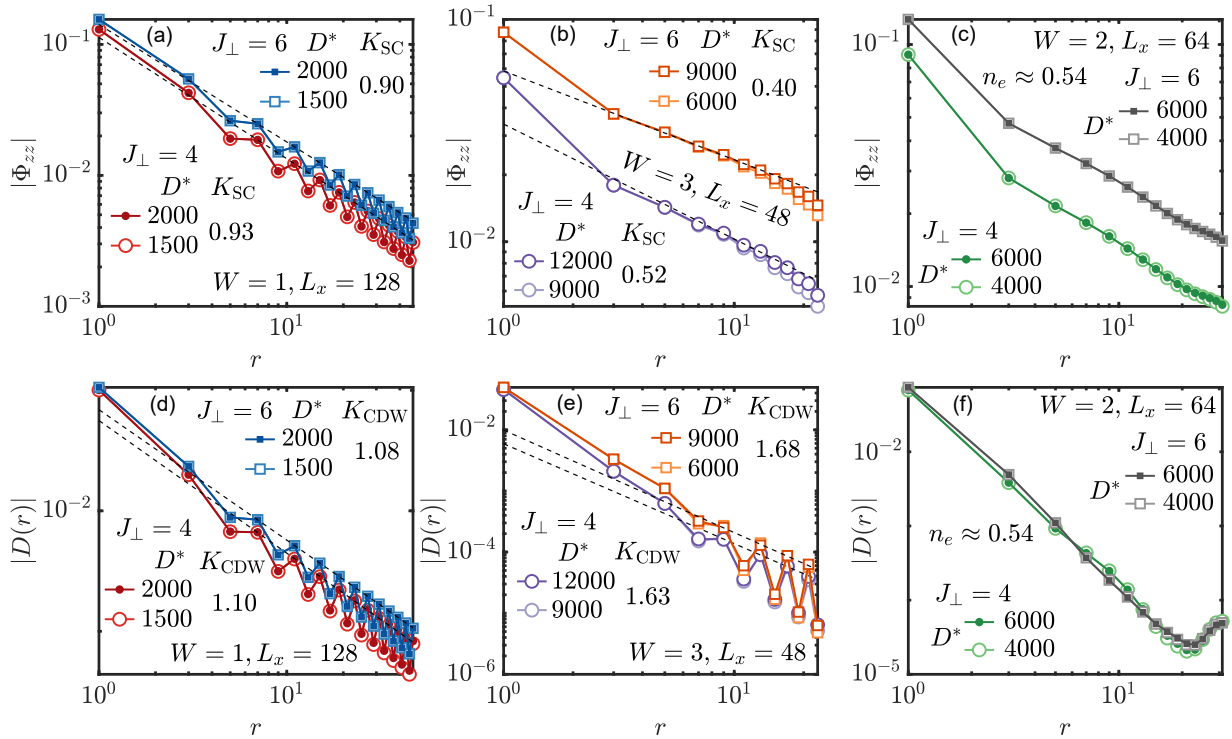


FIG. S2. DMRG results of the $W = 1, 2, 3$ system with two different interlayer couplings $J_{\perp} = 4, 6$. (a, d) pairing correlation and charge correlation for the $W = 1, n_e = 0.5$ system, (b, e) for $W = 3, n_e = 0.5$ system and (c, f) for $W = 2, n_e \approx 0.54$ system.

$C(1/D^*) = C(0) + a/D^* + b/D^{*2}$ and extrapolate the data to infinite D^* . With this we obtain an accurate estimation of K_{SC} and K_{CDW} indicated in Fig. S1(c,f). Since the DMRG simulations converge faster on $J_{\perp} = 4, 6$ systems, we did not extrapolate the data and rely on the well converged segment to extract the Luttinger parameters.

W = 2 case.— The results of $W = 2$ case are shown in Figs. S1(d,g) (for $J_{\perp} = 2$) and S2(c,f) (for $J_{\perp} = 4, 6$). Firstly, we point out that there has a subtlety at exact quarter-filling (i.e., $n_e = 0.5$). The pair correlations computed on the $L_x = 32$ system turn out to decay exponentially when extending the calculations to longer systems [grey lines in Fig. S1(d,g)]. An explanation for this phenomenon could be that the system is being viewed as two coupled t - J ladders with a finite charge gap at quarter filling, as reported in Ref. [44]. Therefore, we fine tune the electron density to $n_e \simeq 0.51$ - 0.56 for the $W = 2$ case in Figs. S1(d,g) and S2(c,f), in order to avoid the peculiar filling $n_e = 0.5$ for the $W = 2$ geometry. In Figs. S1(d) and S2(c), we now observe robust superconductivity for the $W = 2$ case. It is worth noting that the chosen $n_e \gtrsim 0.5$ is actually more closely related to the realistic electron density in the $d_{x^2-y^2}$ orbital due to the self-doping [13, 17], and it also leads to more consistent results for different widths W [as can be seen in Fig. 3(b) in the main text].

CDW correlations.— In Fig. S1(e,f,g) and Fig. S2(d,e,f) we also show results of the charge correlations. For the $W = 1$ case ($J_{\perp} = 2$), we find in Fig. S1(e) that the density correlation $D(r) = \langle n(i)n(i+r) \rangle - \langle n(i) \rangle \langle n(i+r) \rangle$ exhibits a power-law scaling with Luttinger parameter $K_{CDW} \simeq 1.13$. Moreover, we find the product of two Luttinger parameters $K_{SC} K_{CDW} = 1.08 \approx 1$, which fulfills the expectation of the LE theory. Likewise, the $W = 1, J_{\perp} = 4, 6$ cases shown in Fig. S2(a, d) also meet $K_{SC} K_{CDW} \approx 1$. However, for wider systems, such as the $W = 3, J_{\perp} = 2$ case shown in Fig. S1(f) and $W = 3, J_{\perp} = 4, 6$ case in Fig. S2(e), we find that the extracted K_{CDW} is much larger than the SC parameter K_{SC} . This indicates a uniform SC order with relatively weak CDW correlations in wider systems, suggestive of a robust SC order in the 2D limit. Regarding the $W = 2$ case, either for $J_{\perp} = 2$ [Fig. S1(g)] or $J_{\perp} = 4, 6$ [Fig. S2(f)], we see strong oscillations and quite difficult to extract the Luttinger exponent K_{CDW} there.

B. iPEPS method

To simulate the t - J - J_{\perp} model directly in the thermodynamic limit, we flatten the bilayer system into a single layer system with enlarged local Hilbert space and use the fermionic iPEPS method [22, 45–47]. The wavefunction ansatz is illustrated in Fig. S3(a), with a 2×2 unit cell consisting of two bulk tensors (see inset of Fig. S7 below). Each bulk tensor has four

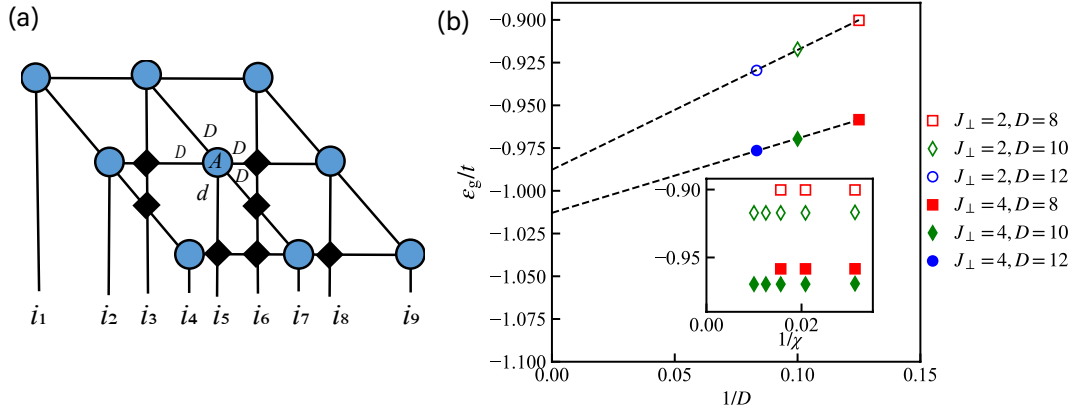


FIG. S3. (a) Illustration of fermionic iPEPS ansatz used in our calculations, where the local tensors (blue solid circles) and the swap gates (black diamonds) taking care of the fermion sign are indicated. D and d represent the bond dimensions of the geometric and physical indices. (b) Energy per site ε_g/t obtained by iPEPS as a function of the inverse bond dimension $1/D$, the environment bond dimension is chosen as $\chi = D^2$. The inset shows the convergence of ε_g/t as a function of $1/\chi$ for various bond dimension D . Other model parameters are $J = 1$ and $t = 3$.

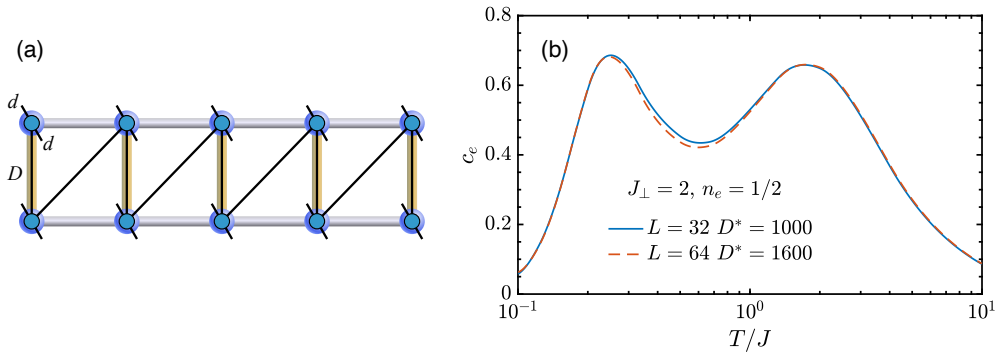


FIG. S4. (a) In tanTRG calculations, we map the $2 \times 1 \times L$ system to a quasi-1D one along the zigzag path. The thermal density operator is represented as an MPO, which consists of rank-4 tensors with two geometric indices with bond dimension D and two physical indices with bond dimension $d = 3$. (b) Electron specific heat c_e for the $2 \times 1 \times L$ systems with $J_\perp = 2$ and electron density $n_e = 1/2$. Results computed with different system sizes and bond dimensions are compared, i.e., $L = 32$ and $D^* = 1000$ (multiples, equivalent $D \simeq 2200$ individual states) vs $L = 64$ and $D^* = 1600$ ($D \simeq 3600$). We find they agree with each other, showing very good convergence over the system sizes and bond dimensions.

virtual bonds whose dimension D can control the simulation accuracy (up to $D = 12$ in practice). It also has a physical bond representing $d = 9$ local electron configurations on the flattened single-layer system. We optimize the iPEPS wavefunction using simple update [22, 37, 38] and the expectation values are calculated using corner transfer matrix renormalization group method [41, 48] with environment bond dimension $\chi = D^2$ that leads to converged results as shown in the inset of Fig. S3(b). It also shows that the energy per site ε_g/t approaches infinite- D limit linearly with $1/D$ for both $J_\perp = 2$ and $J_\perp = 4$ cases.

C. tanTRG method

To simulate the finite-temperature properties of the bilayer systems, we use the tangent-space tensor renormalization group (tanTRG) approach [26], which is a state-of-the-art finite- T approach for many-electron problems. In this approach, the system is mapped to quasi-one-dimensional geometry, and the thermal density operator is represented as a matrix product operator (MPO), as shown in Fig. S4(a). In practical calculations, the Abelian and non-Abelian symmetries are implemented with the QSpace library [33, 34]. To compute the specific heat, magnetic susceptibility, and various electron correlations, we implement $U(1)_{\text{charge}} \times SU(2)_{\text{spin}}$ symmetry and keep up to $D^* = 1600$ multiplets on systems up to $L = 64$. To compute the pairing susceptibility χ_{SC} , we have added a small pairing field, which breaks the particle number conservation. Therefore, we use $\mathbb{Z}_{2,\text{charge}} \times SU(2)_{\text{spin}}$ symmetry and retain up to $D^* = 1000$ multiplets, on long system up to $L = 128$. As the grand canonical

ensemble is used in our thermal tensor network simulations, a chemical potential term $-\mu \sum_i n_i$ is added to fine tune the electron density n_e .

To check the convergence of our thermal data, in Fig. S4(b) we show the electron specific heat c_e results for the $2 \times 1 \times L$ system with $J_\perp = 2$ and electron density $n_e = 1/2$, computed on two different system sizes and bond dimensions: $L = 32$ with $D^* = 1000$, and $L = 64$ with $D^* = 1600$. We find the c_e changes little for the two cases and see a very good convergence of the thermal data.

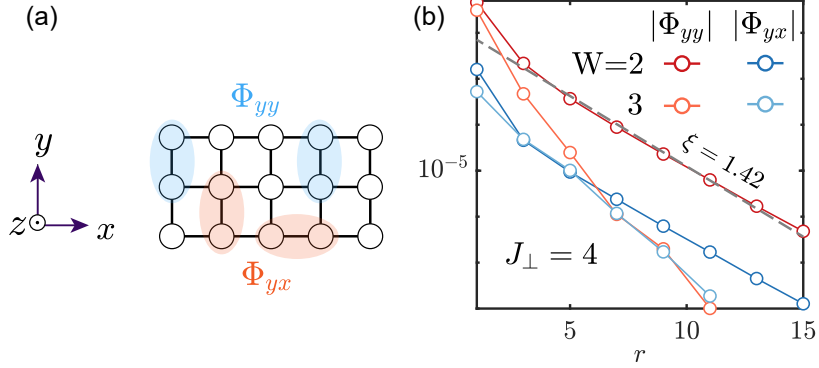


FIG. S5. (a) Schematic of the intralayer pairing correlations $|\Phi_{yy}|$ and $|\Phi_{yx}|$. (b) Intralayer pairing correlations calculated in $2 \times 2 \times 32$ and $2 \times 3 \times 24$ systems, from which we can estimate the correlation length $\xi \simeq 1.42$ for $|\Phi_{yy}|$ on $W = 2$ lattice. Other lines have similar or even shorter correlation lengths.

II. MORE NUMERICAL SIMULATION RESULTS

Below we provide supplemental results obtained with DMRG ($T = 0$, finite system), iPEPS ($T = 0$, thermodynamic limit), and the tanTRG ($T > 0$) calculations.

A. DMRG results

We show in Fig. S5 the intralayer pairing correlation Φ_{yy} and Φ_{yx} on the $2 \times 2 \times 32$ and $2 \times 3 \times 24$ systems. The exponentially decaying pairing correlations indicate the absence of intralayer pairing.

In Fig. S6(a) we find the pairing correlation Φ_{zz} decreases as interlayer AF coupling J_\perp weakens. The rung-single SC order becomes very weak for $J_\perp = 0.1$, supporting our conclusion that the interlayer pairing in the system is mediated by the interlayer AF couplings. In Fig. S6(b) we find the charge density wave (CDW) becomes stronger as the hole density n_h decreases, which is stabilized and even constitutes a long-range pattern for $n_h = 1/16$.

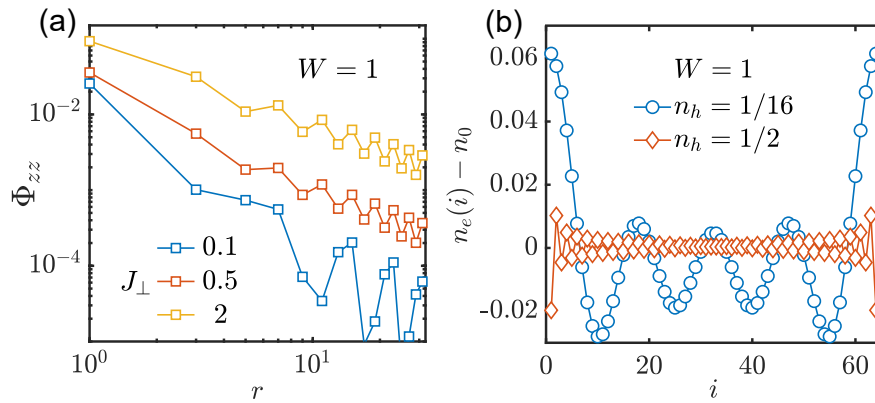


FIG. S6. (a) The pairing correlations Φ_{zz} are shown for different $J_\perp = 0.1, 0.5$ and 2 . (b) The CDW profiles for different hole densities $n_h = 1/2$ and $1/16$.

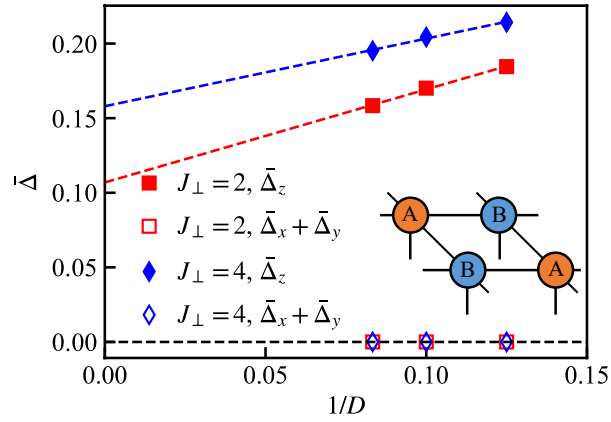


FIG. S7. The rung-singlet SC order parameters obtained by iPEPS are shown as a function of inverse D . $\bar{\Delta}_z$ represents the interlayer pairing along the \hat{z} direction, while $\bar{\Delta}_x$ and $\bar{\Delta}_y$ represent the intralayer pairing along the \hat{x} and \hat{y} directions, respectively. The inset is an illustration of the unit cell of the iPEPS ansatz with two bulk tensors: A and B. Each bulk tensor has one physical bond and four virtual bonds. The $\bar{\Delta}_z$ values are computed and averaged over two bulk tensors, and then extrapolated to infinite D limit. $\bar{\Delta}_z$ has a finite and rather large value, while $|\bar{\Delta}_{x(y)}|$ values are negligibly small.

B. iPEPS results

We show in Fig. S7 the SC order parameter $\bar{\Delta}$ obtained by the iPEPS method in the infinite systems with different J_\perp . The amplitudes of $\bar{\Delta}_z = \frac{1}{\sqrt{2}} \langle \sum_{\mu=\pm 1} c_{i,\mu,\uparrow}^\dagger c_{i,-\mu,\downarrow}^\dagger \rangle$ for both $J_\perp = 2$ and $J_\perp = 4$ decrease with increasing bond dimensions D , while still have very large values when extrapolated to the infinite- D limit. It indicates that the interlayer pairing persists in this limit. On the other hand, we do not find intralayer pairing as the amplitudes of $\bar{\Delta}_x$ and $\bar{\Delta}_y$ are negligible for both J_\perp values, where $\bar{\Delta}_{x(y)} = \frac{1}{\sqrt{2}} \sum_{\sigma=\{\uparrow,\downarrow\}} \langle \text{sgn}(\sigma) c_{i,\mu=\pm 1,\sigma}^\dagger c_{i+\hat{x}(\hat{y}),\mu=\pm 1,\bar{\sigma}}^\dagger \rangle$, with $\text{sgn}(\uparrow) = 1$, $\text{sgn}(\downarrow) = -1$, and $\hat{x}(\hat{y})$ unit vector in the square-lattice plane. $\bar{\sigma}$ reverses the spin orientation of σ . In Fig. S7 we find that $\bar{\Delta}_z$ is enhanced by increasing J_\perp from 2 to 4. The iPEPS results also support the conclusion that a larger J_\perp strengthens the interlayer pairing.

C. tanTRG results

In Fig. 4 of the main text, we have shown the c_e and χ_m for $J_\perp = 2$ with hole density $n_h = 1/2$. Here in Fig. S8(a) we show the c_e and χ_m results for the same $J_\perp = 2$ but with smaller hole density $n_h = 1/4$. Now the low-temperature peak of c_e is found to be located at $T_l/J \simeq 0.38$, and the hump of χ_m is at $T_m/J \simeq 0.75$. Both temperature scales are higher than the corresponding values in the quarter filling ($n_h = n_e = 1/2$) case shown in Fig. 4 of the main text.

In Fig. S8(b) we show the pairing susceptibility χ_{SC} for $J_\perp = 2$ and hole density $n_h = 1/4$, and compare it to the $n_h = 1/2$ case. We find there is an overall enhancement in χ_{SC} when n_h is lowered from $1/2$ to $1/4$. Moreover, the characteristic temperature scale T_c^* for superconductivity increases from $T_c^*/J \simeq 0.12$ to 0.16 . Therefore, compared with quarter filling case with $n_h = 1/2$ (pristine $\text{La}_3\text{Ni}_2\text{O}_7$), the superconductivity is enhanced by lowering hole density ($n_h = 1/4$).

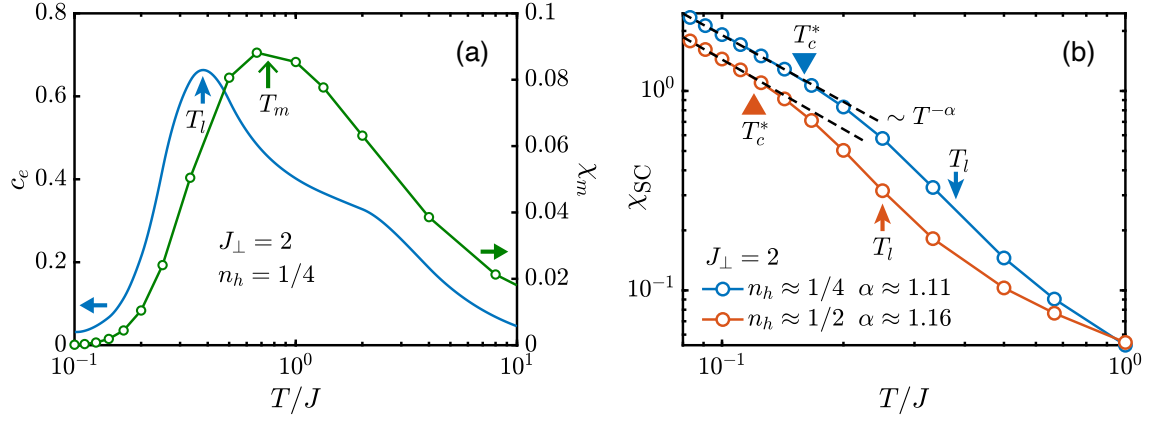


FIG. S8. (a) Specific heat c_e and magnetic susceptibility χ_m for the $2 \times 1 \times 32$ system with $J_{\perp} = 2$ and hole density $n_h = 1/4$. The blue upward arrow indicates the lower temperature scale in c_e . The green upward arrow indicates the peak temperature of χ_m . (b) Pairing susceptibility for the $2 \times 1 \times 128$ system with $J_{\perp} = 2$ and $n_h = 1/4, 1/2$. The $n_h = 1/2$ data is exactly the same one as in Fig. 4(b) of the main text, taken here as a comparison. The dashed lines denote the power-law fitting $T^{-\alpha}$. The corresponding temperature scales T_c^* and T_l are indicated.